MicMec: Developing the Micromechanical Model to Investigate the Mechanics of Correlated Node Defects in UiO-66

Joachim Vandewalle, Juul S. De Vos, and Sven M. J. Rogge*

Center for Molecular Modeling (CMM), Ghent University,

Technologiepark-Zwijnaarde 46, B-9052 Zwijnaarde, Belgium

E-mail: Sven.Rogge@UGent.be

Abstract

New functional materials, such as mixed matrix membranes and metal-organic framework (MOF) monoliths, outperform traditional materials in gas separation and storage applications, among other pressing challenges. However, while most engineered materials nowadays exhibit spatial heterogeneities on different length scales, available simulation techniques to date cannot capture this spatial complexity fully. Herein, we present the `MicMec` implementation of the micromechanical model we introduced earlier as a systematic coarse-graining approach to routinely access these larger length scales and characterize the mechanical properties of these materials. We thoroughly discuss the key components of our open-source code and validate it both on an analytical system and a case study on correlated **reo** defects in the UiO-66 MOF. We reveal that the timestep that can be reached in micromechanical simulations is two to three orders of magnitude larger than for atomistic simulations, while still capturing well the macroscopic mechanical properties of the spatially disordered UiO-66 material. It is our hope that the `MicMec` implementation discussed here may provide a complementary tool to existing atomistic and coarse-grained software and aid the computational design of new materials for pressing applications.

1 Introduction

Computational material design evolved into a thriving field of research driven by the advent of high-performance computing infrastructure, progress in (open-source) simulation codes and material databases, and the development of highly accurate electronic structure methods and interatomic potentials.[1–6] One of the principal outstanding challenges for computational chemists lies in reconciling structural models of increasingly complex materials with accurate but expensive descriptions of the interparticle interactions in a given material.[6] For instance, consider metal-organic frameworks (MOFs), a diverse class of often highly porous materials composed of organic and inorganic building blocks.[7,8] Their intricate composition and anomalous behavior motivated extensive research to design these materials for applications in, among others, catalysis,[9,10] gas separation,[11,12] and even drinkable water harvesting in arid environments without the need for external energy sources.[13,14] Computational research may speed up identifying interesting MOFs for these and other applications, but only when the considered *in silico* models capture the structural complexity of experimentally synthesized MOFs.[6] This is by no means a straightforward challenge since MOFs exhibit spatial heterogeneities on different length scales—such as the well-documented linker and node vacancies or correlated spatial disorder—and since their macroscopic behavior depends on the size of the MOF crystal.[6,15–20] This multiscale challenge is complicated further when combining MOFs with other materials into structurally complex composites.[21,22] For example, mixed matrix membranes combine the attractive behavior of MOFs with the easier processibility of polymer matrices.[23,24] Current MOF simulation procedures overwhelmingly rely on methods that cannot reach the length scales needed to describe these structural heterogeneities beyond a few tens of nanometers. Therefore, we herein implement the micromechanical model, outlined in ref. 25, into the `MicMec` software and validate this open-source python code. Furthermore, we demonstrate how our simulation code can model the impact of correlated node defects on the mechanical stability of UiO-66(Zr), a prototypical MOF, as an example of how `MicMec` can drive research into structurally complex framework materials.

The majority of current simulation techniques describe the interparticle interactions in a MOF material following one of two approaches: either by treating the material's electronic structure explicitly, such as wave-function-based methods and more popular techniques based on density functional theory (DFT),[5,26] or by approximating the internuclear interactions via classical potentials or force fields.[27] Although such atomic force fields already yield a substantial scale-up in attainable simulation models, they still fall short of the computational efficiency needed to describe MOF models beyond a few tens of nanometers in size. Compared with these two commonly adopted methods, recent developments such as machine-learned potentials,[4,28,29] coarse-grained (CG) force fields,[30–34] and finite element methods[35] have increased the attainable simulation size. Machine-learned potentials achieve this by approximating the electronic interactions, similar to classical interatomic potentials.[4,28,29] However, they do so more accurately than classical potentials by using various machine-learning techniques. As a result, they are able to describe structural models up to the size described by classical force fields while reaching an accuracy comparable to DFT methods. CG force fields and finite element modeling achieve an even more significant scale-up in structural models they can treat. For CG models, this is achieved by grouping atoms in so-called CG beads or CG nodes according to a specified mapping and analytically prescribing the interbead interactions.[30,31,33] Like classical force fields, CG force fields can be developed either top-down, which relies on tuning the model parameters to match experimental observations, or bottom-up, which optimizes the model parameters to best reproduce the atomic free energy surface or derivatives thereof. As CG beads lack internal structure, this approach reduces the degrees of freedom in the system and thus allows one to consider larger models. At the moment, CG work on MOFs is scarce, the only exceptions being the pioneering work of Dürholt *et al.* on HKUST-1[31] and the works of Semino and co-workers on HKUST-1 and, very recently, ZIF-8.[32,34] Finally, finite element methods depart entirely from the atomic structure of MOFs and instead subdivide the material into finite elements whose behavior is dictated by constitutive relations. For instance, Evans *et al.* adopted this approach to

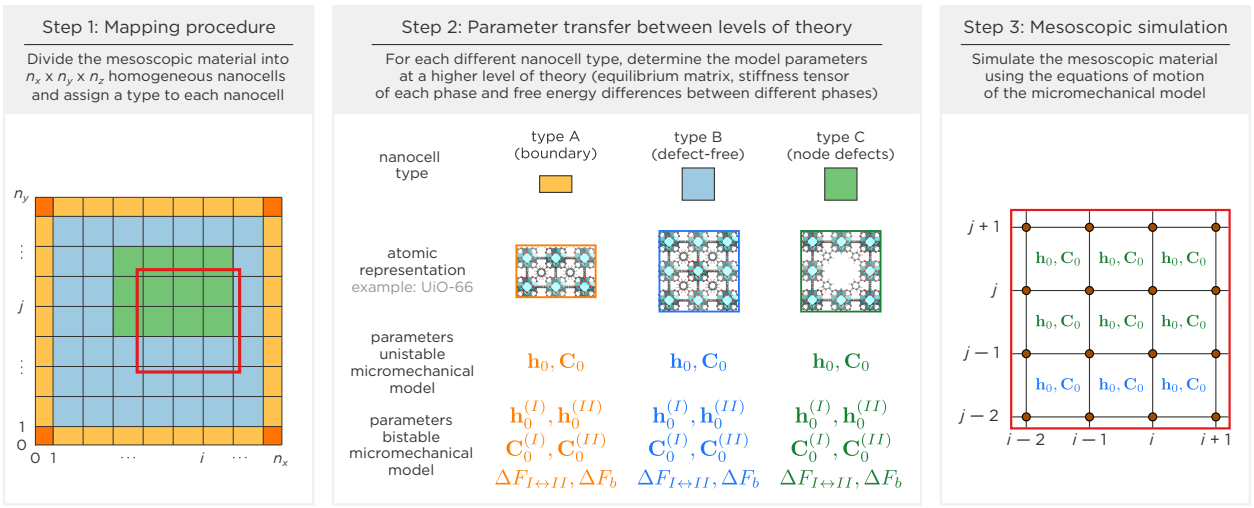

Figure 1: The three steps in the micromechanical model, illustrated for UiO-66 containing nodal defect regions (green), defect-free regions (blue) and surface regions (orange). Step 3 shows a close-up of the model for the region defined by the red rectangle in step 1. Reproduced with permission from ref 25. Copyright 2021 Royal Society of Chemistry.

determine the effective bulk modulus of various MIL-53(Al)-NH_2-containing mixed matrix membranes with sizes of several hundreds of micrometers.[35] Like CG methods or machine-learned potentials, their application to MOFs remains limited to date, and it remains unclear to which extent these approaches are transferable to other materials and geometries.

Inspired by these techniques, some of us introduced the micromechanical model as an intermediate between CG models and finite element methods.[25] This model defines micromechanical CG nodes or beads and the corresponding internode interactions following the three-step approach illustrated in Figure 1. Firstly, the material to be simulated is subdivided into smaller cells that correspond to conventional unit cells or small supercells thereof, which are called nanocells because their cell lengths are within the nanometer range. This approach maps the atomic content of each nanocell to interaction nodes located on the corners of these nanocells. In 3D, each nanocell is hence defined by eight nodes, which can each be shared by a maximum of eight neighboring nanocells. Furthermore, a nanocell type is assigned to each of these different nanocells. This nanocell type indicates their structural content and will define the interactions between the interaction node on the corners of the

nanocell. For instance, for the UiO-66 example of Figure 1, different cell types are introduced for pristine UiO-66 nanocells, node-defective UiO-66 nanocells, and surface-terminated UiO-66 nanocells. Secondly, for each nanocell type, a limited set of parameters are defined that describe how the nodes on the corners of the nanocell interact. These parameters, defined bottom-up by preceding atomic simulations or top-down by mechanical experiments, describe the response of the nanocell upon an external trigger. If a nanocell can only adopt a single phase, the equilibrium cell matrix $\mathbf{h}_0$ and the equilibrium elastic stiffness tensor $\mathbf{C}_0$ are sufficient to describe these interactions in the elastic regime. These parameters incorporate the material's topology, which is a vital descriptor for predicting a material's mechanical response.[36] In case the nanocell can adopt multiple phases, the equilibrium cell matrices and elastic stiffness tensors for each phase are required, as well as the free energy differences between the different phases, ΔF, and the free energy barrier separating each pair of phases, ΔF_b. As outlined in ref. 25, this free energy barrier can also be defined through an effective temperature T^*. For unistable and multistable phases alike, the amount of hierarchical parameters defined in this way scales only with the number of different nanocell types. Thirdly, this information is used to simulate how the mesoscopic material responds to external triggers. To this end, the positions of each micromechanical bead are adopted to define the different instantaneous nanocell matrices $\mathbf{h}_{\kappa\lambda\mu}$ throughout the mesoscopic material. By comparing this instantaneous cell matrix with the equilibrium matrix for that nanocell type, the 3×3 Lagrangian strain tensor $\boldsymbol{\varepsilon}_{\kappa\lambda\mu}$ can be defined for each nanocell.[37,38] Together with the elastic stiffness tensor, this defines the potential deformation energy $\mathcal{U}_{\kappa\lambda\mu}$ needed to adopt this specific configuration of micromechanical nodes in the given nanocell. Summing this potential deformation energy for each nanocell and taking the derivative with respect to each micromechanical bead's position results in the total force acting on that bead which can be used to update the equations of motion in a micromechanical simulation.

The micromechanical model's focus on the elastic deformation energy is reminiscent of the landmark works of Triguero *et al.*, in which a model Hamiltonian was introduced to

investigate the adsorption-induced breathing in MIL-53.[39,40] In their approach, the Hamiltonian of the guest-free framework also contained a local deformation energy contribution, which, however, depended on a scalar strain metric and an effective elastic constant as a fitting parameter. Furthermore, their Hamiltonian was supplemented with a non-local elastic energy depending on the gradient of this strain and an interfacial energy fitting parameter. In contrast, our micromechanical model is parametrized by the experimentally verifiable stiffness tensor, which makes it easier to transfer the approach to other systems. Moreover, the nonlocality of the deformation energy, *i.e.*, the fact that the deformation of one cell may affect neighboring cells, is an inherent part of our micromechanical model since the grid of interaction nodes and the grid of cells are staggered with respect to one another. As a result, if one node moves from its equilibrium position, it deforms all cells surrounding this node without the need for extra terms in our Hamiltonian. The micromechanical model also fundamentally departs from the more traditional CG techniques for MOFs mentioned above.[31,32,34] In the micromechanical model, the internode interactions are determined by unit cell properties—the unit cell matrix and elastic stiffness tensor—rather than fitted to reproduce the interactions in, and configurations of, atomic models. This not only circumvents the need for tedious parameter fitting, but may also improve reproducing the mechanical properties in our CG model.

While we postulated this micromechanical workflow and the associated equations of motion in ref. 25, the validation of the model and different fundamental questions remained unresolved up to this point. Firstly, mapping the different atoms onto the heavier micromechanical nodes that define the nanocells averages out high-frequency motions. Nevertheless, it needs to be quantified to what extent this increases the maximum timestep to be used in a molecular simulation while still satisfying the Nyquist sampling criterion and reliably sampling the interbead interactions. Secondly, the transformation from the micromechanical nodes to the instantaneous nanocell matrix is non-bijective. As a result, multiple bead configurations can give rise to the same nanocell matrix in the original micromechanical model.

This should be fine as long as the nodes remain close to their original positions. However, it remains to be investigated if and when this non-bijective character poses problems in defining representative instantaneous nanocell matrices. Thirdly and most importantly, the lack of an easily interpretable and open-source software code that incorporates the micromechanical model hampers the adoption and further development of the micromechanical model as an alternative approach, next to traditional CG and finite elements methods.

In this work, we answer these questions by implementing the micromechanical model into the open-source `MicMec` code. Besides validating our implementation through analytical examples, we also investigate through the micromechanical model how the concentration and distribution of node defects alter the mechanical properties of UiO-66(Zr) materials.[41] UiO-66(Zr) is chosen here as a prototypical MOF exhibiting spatial disorder on different length scales.[15,16,42–49] Techniques such as transmission electron microscopy and single-crystal X-ray diffraction revealed that the spatial disorder in these materials, such as linker and node vacancies, are strongly correlated and give rise to local domains in which the material adopts **bcu**, **reo**, or **scu** nets within the pristine **fcu** matrix.[15,16] Given the experimental prevalence of **reo** node defects in the otherwise **fcu** material, we will herein vary the **reo**:**fcu** concentration as well as the distribution of the **reo** cells inside the parent **fcu** material and validate in how far our `MicMec` implementation succeeds in predicting how this impacts the mechanical behavior of these structures. We hope that this validation and the availability of the open-source `MicMec` code may provide the computational material design community with a complementary tool to investigate increasingly complex framework materials.

2 Theoretical methods

Before discussing the validation of the micromechanical model, this section will give an overview of its implementation in the `MicMec` software. We will firstly focus on an aspect that was not discussed when we first proposed the micromechanical model in ref. 25: the need

to introduce different representations to resolve potential non-uniqueness problems that arise when defining nanocell matrices in a non-bijective way, based on the positions of the eight micromechanical nodes surrounding each nanocell. The actual implementation of the `MicMec` workflow builds on four core routines: the `System` object that connects the micromechanical nodes and nanocells, the `MicMecForceField` object that defines the elastic deformation energy and associated micromechanical forces, and the `Optimizer` and `VerletIntegrator` objects used to perform optimizations and molecular dynamics simulations, respectively. We refer the interested reader to Section S2 in the Supporting Information for more information about these core routines. Together with the documentation provided in the corresponding GitHub repository at `https://jlvdwall.github.io/micmec/`, this workflow should make it possible to adopt the code for any system of interest. This section concludes with the computational details used in this work.

2.1 `MicMec`: Implementation of the micromechanical model

At the core of the micromechanical model lies the elastic deformation energy $\mathcal{U}_{\kappa\lambda\mu}$ experienced by a nanocell with indices (κ, λ, μ) when it is deformed from its equilibrium cell matrix $\mathbf{h}_{\kappa\lambda\mu,0}$ to an instantaneous cell matrix $\mathbf{h}_{\kappa\lambda\mu}$. To this end, we defined the 3×3 Lagrangian strain tensor[37,38]

$$\boldsymbol{\varepsilon}_{\kappa\lambda\mu} = \frac{1}{2}\left[\mathbf{h}_{\kappa\lambda\mu,0}^{-T}\mathbf{h}_{\kappa\lambda\mu}^{T}\mathbf{h}_{\kappa\lambda\mu}\mathbf{h}_{\kappa\lambda\mu,0}^{-1} - \mathbf{1}\right], \tag{1}$$

in which $\mathbf{a}^T$ and $\mathbf{a}^{-1}$ are the transpose and inverse of the matrix $\mathbf{a}$, $\mathbf{a}^{-T} = (\mathbf{a}^{-1})^T = (\mathbf{a}^T)^{-1}$, and $\mathbf{1}$ is the unit tensor of rank two. In this expression, only the cell matrix $\mathbf{h}_{\kappa\lambda\mu}$ and its transpose change during a simulation. This allowed us to define the deformation energy of that nanocell at each time instant as[50]

$$\mathcal{U}_{\kappa\lambda\mu} = \frac{V_{\kappa\lambda\mu,0}}{2}\boldsymbol{\varepsilon}_{\kappa\lambda\mu}^{T} : \mathbf{C}_{\kappa\lambda\mu,0} : \boldsymbol{\varepsilon}_{\kappa\lambda\mu}, \tag{2}$$

with $\mathbf{a} : \mathbf{b} = \sum_{ij} a_{ij} b_{ij}$ denoting a double tensor contraction. At this stage, it is important to point out that the factor $V_{\kappa\lambda\mu,0}$ in Eq. 2, which indicates the equilibrium cell volume $V_{\kappa\lambda\mu,0} = \det \mathbf{h}_{\kappa\lambda\mu,0}$, replaces the *instantaneous* cell volume $V_{\kappa\lambda\mu} = \det \mathbf{h}_{\kappa\lambda\mu}$ used in our original formulation.[25] The current formulation of Eq. 2 corresponds with the first non-vanishing term when expanding the Helmholtz free energy $F(\boldsymbol{\varepsilon})$ as a function of the strain around the unstrained equilibrium state.[50] It is therefore the formulation that should be used to define the deformation energy, as this is the coarse-grained potential energy surface on which our micromechanical nodes will move. While the difference between using the equilibrium and the instantaneous nanocell volume is small near equilibrium, our UiO-66 simulations show that using the instantaneous volume may lead to artifacts when reducing the nanocell volume by more than 10%, as outlined in Section S1 of the Supporting Information. Furthermore, using Eq. 2 simplifies the resulting equations of motion, since only the two strain tensors $\boldsymbol{\varepsilon}_{\kappa\lambda\mu}$ depend on the positions of the different nodes.

Given the relations between the cell matrix, strain, and deformation energy for any given nanocell given in Eqs. 1 and 2, the only open question at this point is how to define the nanocell matrix $\mathbf{h}_{\kappa\lambda\mu}$ from the eight micromechanical nodes at positions $\boldsymbol{r}_{klm}$ that surround it. In what follows, we will denote this set of eight nodes that define the nanocell at index (κ, λ, μ) by $\mathcal{S}_{\kappa\lambda\mu}$, so that the eight nodal positions are collectively given by $\{\boldsymbol{r}_{klm}\}_{\mathcal{S}_{\kappa\lambda\mu}}$. We will also use Latin letters to indicate nodal indices and distinguish them from the Greek letters used for nanocell indices. Naively, one could be tempted to define the nanocell matrix by defining the twelve internodal vectors connecting adjacent nodes, as in the top pane of Figure 2, and by averaging over each group of four vectors that would be equivalent in a parallelepiped. However, in general, the positions of the eight micromechanical nodes $\{\boldsymbol{r}_{klm}\}_{\mathcal{S}_{\kappa\lambda\mu}}$ are arbitrary and do not need to form a perfect parallelepiped. In that case, this naive averaging procedure will smoothen out local deviations in the positions of the micromechanical nodes. For instance, consider the two nodal configurations in the top right pane of Figure 2. In the top nanocell, one node strongly deviates from the cubic positions

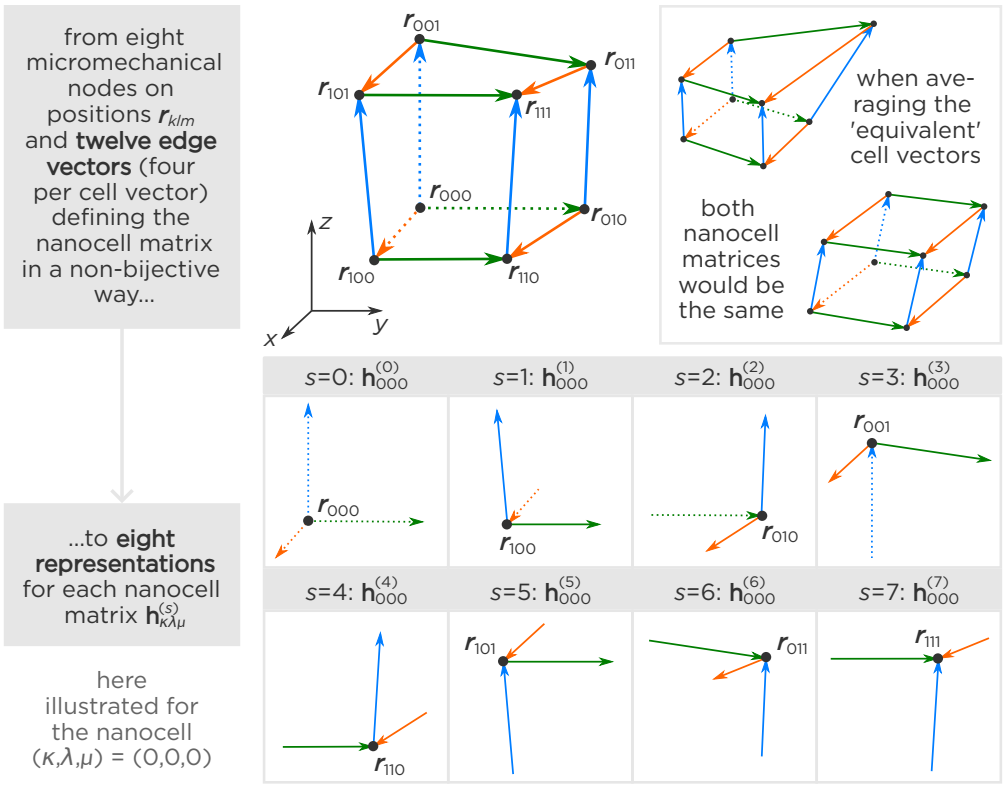

Figure 2: Any nanocell matrix $\mathbf{h}_{\kappa\lambda\mu}$ is defined by the positions of the micromechanical nodes that surround it, $\{\boldsymbol{r}_{klm}\}_{\mathcal{S}_{\kappa\lambda\mu}}$. Naively, one could construct this matrix by averaging, for each of three cell vectors, over the four equivalent definitions of this cell vector, which are indicated by the same color in the upper panel. However, due to the non-bijectiveness of this operation, the resulting nanocell matrix may not represent the actual nodes well. The two distinct node configurations in the top right inset exemplify this, as they would yield the same averaged nanocell matrix. Therefore, we define in the lower pane eight representations $\mathbf{h}^{(s)}_{\kappa\lambda\mu}$ for each nanocell with index (κ, λ, μ). Each representation s corresponds to one of the eight micromechanical nodes surrounding the nanocell and properly considers the energy needed to deform the node to that position.

adopted by the other seven nodes, which results in strong deviations within each group of four 'equivalent' cell vectors. However, by averaging over each group, the average cell vectors of this first nanocell completely coincide with those of the second nanocell beneath it, which is a perfect parallelepiped. One cannot expect both deformations to require the same deformation energy, which implies that a different approach should be adopted to define the nanocell matrix $\mathbf{h}_{\kappa\lambda\mu}$ from its surrounding micromechanical nodes $\{\boldsymbol{r}_{klm}\}_{\mathcal{S}_{\kappa\lambda\mu}}$.

To solve this non-bijectiveness between the micromechanical nodes and the nanocells they

define, we opted to work with different representations $\mathbf{h}^{(s)}_{\kappa\lambda\mu}$ for each nanocell matrix $\mathbf{h}_{\kappa\lambda\mu}$ in `MicMec`. Each representation corresponds to one of eight corners of the nanocell, as indicated in Figure 2, and considers the three vectors of the specified nanocell that arrive in, or depart from, that node. In this way, when some micromechanical nodes deviate strongly from their equilibrium positions, they will also induce strong deviations in some of the nanocell matrix representations $\mathbf{h}^{(s)}_{\kappa\lambda\mu}$, with $s \in \{0, 1, 2, 3, 4, 5, 6, 7\}$. In turn, for each nanocell representation, a distinct strain tensor can be defined:

$$\boldsymbol{\varepsilon}^{(s)}_{\kappa\lambda\mu} = \frac{1}{2}\left[\mathbf{h}^{-T}_{\kappa\lambda\mu,0}\left(\mathbf{h}^{(s)}_{\kappa\lambda\mu}\right)^{T}\mathbf{h}^{(s)}_{\kappa\lambda\mu}\mathbf{h}^{-1}_{\kappa\lambda\mu,0} - \mathbf{1}\right], \tag{3}$$

which in turn leads to eight different deformation energies for each nanocell:

$$\mathcal{U}^{(s)}_{\kappa\lambda\mu} = \frac{V_{\kappa\lambda\mu,0}}{2}\left(\boldsymbol{\varepsilon}^{(s)}_{\kappa\lambda\mu}\right)^{T} : \mathbf{C}_{\kappa\lambda\mu,0} : \boldsymbol{\varepsilon}^{(s)}_{\kappa\lambda\mu}. \tag{4}$$

In contrast to the naive averaging procedure, a deformation in one node will here result in large deformation energies for some representations. By defining the total deformation energy of a given nanocell as the average over the eight different representations for that cell,

$$\mathcal{U}_{\kappa\lambda\mu} = \frac{1}{8}\sum_{s=0}^{7}\mathcal{U}^{(s)}_{\kappa\lambda\mu}, \tag{5}$$

this `MicMec` procedure ensures that the total deformation energy does take these local deviations into account.

Following our original procedure, the force acting on the micromechanical node with index (k, l, m) can now be defined by taking the derivative of the total deformation energy of the system $\mathcal{U}_{\text{sys}}$—obtained by summing Eq. 5 over each nanocell—with respect to that node's position. By defining $\mathcal{S}_{klm}$ as the set of eight nanocells that surround the node with

index (k,l,m), we can determine this force as

$$\boldsymbol{f}_{klm} = -\nabla_{\boldsymbol{r}_{klm}} \mathcal{U}_{\text{sys}} = -\sum_{(\kappa,\lambda,\mu)\in\mathcal{S}_{klm}} \nabla_{\boldsymbol{r}_{klm}} \mathcal{U}_{\kappa\lambda\mu} = -\frac{1}{8} \sum_{(\kappa,\lambda,\mu)\in\mathcal{S}_{klm}} \sum_{s=0}^{7} \nabla_{\boldsymbol{r}_{klm}} \mathcal{U}^{(s)}_{\kappa\lambda\mu}. \tag{6}$$

For further use in the `MicMec` code, we will also define the force acting on node (k,l,m) due to representation s of nanocell (κ,λ,μ) as

$$\begin{aligned} \boldsymbol{f}_{klm}|^{(s)}_{\kappa\lambda\mu} &= -\nabla_{\boldsymbol{r}_{klm}} \mathcal{U}^{(s)}_{\kappa\lambda\mu} \\ &= -\frac{V_{\kappa\lambda\mu,0}}{2} \left[\left(\nabla_{\boldsymbol{r}_{klm}} \left(\boldsymbol{\varepsilon}^{(s)}_{\kappa\lambda\mu} \right)^T \right) : \mathbf{C}_{\kappa\lambda\mu,0} : \boldsymbol{\varepsilon}^{(s)}_{\kappa\lambda\mu} + \left(\boldsymbol{\varepsilon}^{(s)}_{\kappa\lambda\mu} \right)^T : \mathbf{C}_{\kappa\lambda\mu,0} : \left(\nabla_{\boldsymbol{r}_{klm}} \boldsymbol{\varepsilon}^{(s)}_{\kappa\lambda\mu} \right) \right] \end{aligned} \tag{7}$$

Finally, the gradients of the strain defined in Eq. 7 can be evaluated by inserting Eq. (3):

$$\nabla_{\boldsymbol{r}_{klm}} \left(\boldsymbol{\varepsilon}^{(s)}_{\kappa\lambda\mu} \right)^T = \nabla_{\boldsymbol{r}_{klm}} \boldsymbol{\varepsilon}^{(s)}_{\kappa\lambda\mu} = \frac{1}{2} \mathbf{h}^{-T}_{\kappa\lambda\mu,0} \left[\nabla_{\boldsymbol{r}_{klm}} \left(\mathbf{h}^{(s)}_{\kappa\lambda\mu} \right)^T \mathbf{h}^{(s)}_{\kappa\lambda\mu} + \left(\mathbf{h}^{(s)}_{\kappa\lambda\mu} \right)^T \nabla_{\boldsymbol{r}_{klm}} \mathbf{h}^{(s)}_{\kappa\lambda\mu} \right] \mathbf{h}^{-1}_{\kappa\lambda\mu,0}. \tag{8}$$

2.2 Computational details

In what follows, two types of systems are considered. Firstly, the `MicMec` model will be validated using an analytical and homogeneous test system, for which the unique cell matrix and elastic stiffness tensor in equilibrium are postulated as

$$\mathbf{h}^{\text{test}}_0 = \begin{bmatrix} 10 & 0 & 0 \\ 0 & 10 & 0 \\ 0 & 0 & 10 \end{bmatrix} \text{Å} \qquad \mathbf{C}^{\text{test}}_0 = \begin{bmatrix} 50 & 30 & 30 & 0 & 0 & 0 \\ 30 & 50 & 30 & 0 & 0 & 0 \\ 30 & 30 & 50 & 0 & 0 & 0 \\ 0 & 0 & 0 & 10 & 0 & 0 \\ 0 & 0 & 0 & 0 & 10 & 0 \\ 0 & 0 & 0 & 0 & 0 & 10 \end{bmatrix} \text{GPa}. \tag{9}$$

A mass $m = 10^7 m_e$ is assigned to each node, with m_e the electron mass. While the magnitude of the node mass is arbitrary in our test system, we were inspired by the rounded unit cell mass of a conventional UiO-66 unit cell ($m = 1.21 \times 10^7 m_e$). This simple, homogeneous test system is chosen because its equilibrium state is well-known. The elastic stiffness tensor corresponds to a cubic system that satisfies the Born stability criteria in equilibrium.[51,52] This system will be adopted to compare the potential deformation energy induced by and the force acting on a single displaced node when calculated either analytically or through the `MicMec` implementation. In addition, also the bulk modulus of this test system will be validated by performing a relaxed energy scan, as implemented in the `Optimizer` object. In this relaxed scan, the volume of the test system is changed by small increments and a full optimization of the micromechanical nodes is performed. This allows us to record the total potential energy $\mathcal{U}_{\text{sys}}$ of the system as a function of the volume around its equilibrium value $V_0 = \det \mathbf{h}_0$, from which the bulk modulus follows as

$$K = V_0 \left. \frac{\partial^2 \mathcal{U}_{\text{sys}}}{\partial V^2} \right|_{V_0} = \left. \frac{\partial^2 (\mathcal{U}_{\text{sys}}/V_0)}{\partial (V/V_0)^2} \right|_{V_0} \tag{10}$$

This same system is also adopted to test the gain in maximum timestep during an (N, V, E) simulation implemented in the `VerletIntegrator` object, by keeping track of the total energy of the system, which should remain conserved.

Secondly, we also validated our `MicMec` model on a real-life example. To this end, we constructed various periodic micromechanical UiO-66 models containing a combination of pristine **fcu** and node-defective **reo** nanocells. The input parameters for these nanocell types are defined by preceding atomic force field optimizations using the force fields of ref. 53. All optimizations on the atomic level were performed on a $1 \times 1 \times 1$ system with the conjugate gradient algorithm implemented in `Yaff`,[54] using the default convergence criteria (`dpos_rms = 1e-4` and `gpos_rms = 1e-6`). The equilibrium cell matrices of the **fcu** type and the **reo** type were obtained by simultaneously optimizing the atomic coordinates and

the cell parameters, yielding the following equilibrium cell matrices:

$$\mathbf{h}_0^{\mathbf{fcu}} = \begin{bmatrix} 21.0 & -0.4 & 0.6 \\ 0.4 & 21.0 & 0.0 \\ -0.6 & 0.0 & 21.0 \end{bmatrix} \text{Å} \qquad \mathbf{h}_0^{\mathbf{reo}} = \begin{bmatrix} 21.0 & 0.2 & -0.1 \\ -0.2 & 21.0 & -0.3 \\ 0.1 & 0.3 & 21.0 \end{bmatrix} \text{Å} \tag{11}$$

To obtain the equilibrium stiffness tensors, a set of twenty-four optimizations were performed for both the **fcu** and **reo** nanocell types: four for each of the six deformation modes of a crystal. The deformation modes were simulated by imposing a fixed finite strain on the system during a full optimization of the atomic coordinates. As stated by Hooke's law, strain in a system around equilibrium is directly related to stress, which is measured by the virial tensor of the optimized atomic system. By performing four simulations with different strain values of any given deformation mode, an estimate of the elasticity value for that mode can be obtained, following the procedure outlined in ref. 55. The following elastic stiffness tensors were found:

$$\mathbf{C}_0^{\mathbf{fcu}} = \begin{bmatrix} 46.0 & 18.0 & 18.0 & 0.0 & 0.0 & 0.0 \\ 18.0 & 46.0 & 18.0 & 0.0 & 0.0 & 0.0 \\ 18.0 & 18.0 & 46.0 & 0.0 & 0.0 & 0.0 \\ 0.0 & 0.0 & 0.0 & 16.8 & 0.0 & 0.0 \\ 0.0 & 0.0 & 0.0 & 0.0 & 16.8 & 0.0 \\ 0.0 & 0.0 & 0.0 & 0.0 & 0.0 & 16.8 \end{bmatrix} \text{GPa}, \tag{12}$$

$$\mathbf{C}_0^{\mathbf{reo}} = \begin{bmatrix} 23.0 & 9.4 & 9.4 & 0.0 & 0.0 & 0.0 \\ 9.4 & 23.0 & 9.4 & 0.0 & 0.0 & 0.0 \\ 9.4 & 9.4 & 23.0 & 0.0 & 0.0 & 0.0 \\ 0.0 & 0.0 & 0.0 & 8.4 & 0.0 & 0.0 \\ 0.0 & 0.0 & 0.0 & 0.0 & 8.4 & 0.0 \\ 0.0 & 0.0 & 0.0 & 0.0 & 0.0 & 8.4 \end{bmatrix} \text{GPa.} \quad (13)$$

These equilibrium cell matrices and elastic stiffness tensors were used as input for the different micromechanical models discussed hereafter. For each **fcu**:**reo** micromechanical model, the full elastic stiffness tensor was defined by measuring stress-strain relations from a set of twenty-four optimizations, analogous to the atomic workflow discussed above. From the full elastic stiffness tensor, the eigenvalues and corresponding eigenvectors are determined and the directional Young modulus is calculated.

3 Results

3.1 Analytical validation of the micromechanical model

As a first validation of the micromechanical model, we sought to test whether the proposed micromechanical forces of Eqs. 6 and 7 are derived correctly. To do so, we constructed a micromechanical model consisting of $2 \times 2 \times 2$ nanocells of the 'test' type, outlined in the computational details section. Given that periodic boundary conditions are adopted, this micromechanical model consists of eight distinct nodes, as shown in Figure 3a. Because of the homogeneity of this specific model and the equilibrium cell matrix of the test nanocell, no internal forces are acting on the system when the nodes lie on a cubic grid with a spacing of 10 Å. In this configuration, the total deformation energy equals zero.

When moving one of the micromechanical nodes from its equilibrium position while

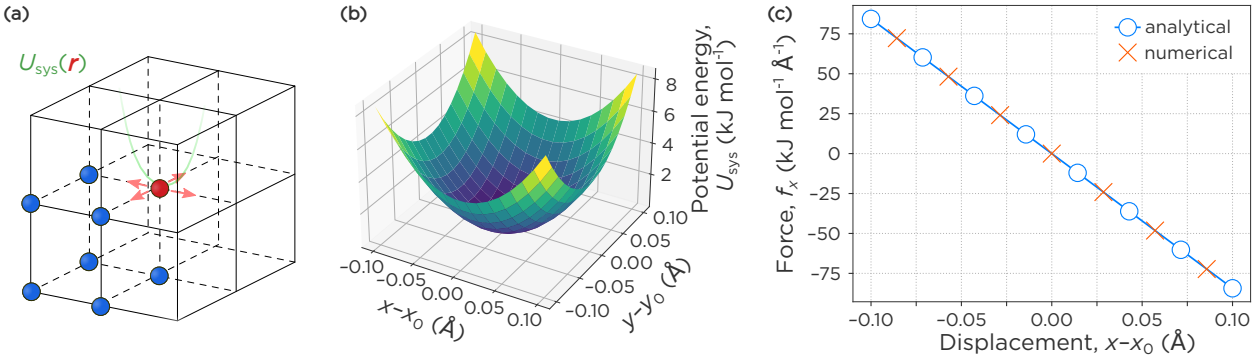

Figure 3: Validation of the `MicMec` implementation using the test system. **(a)** The $2 \times 2 \times 2$ test system with periodic boundary conditions, containing eight distinct nodes. Seven of these nodes are kept fixed, while the eighth is displaced. **(b)** Static energy scan $\mathcal{U}_{\text{sys}}(\boldsymbol{r})$ obtained by displacing one node in pane (a) along the x or y direction. Given the system's symmetry, any displacement along the x, y, or z direction will give the same deformation energy. **(c)** Comparison of the negative numerical gradient of the total potential energy of pane (b) with the analytical expression of the force acting on the node, given in Eq. 6, for various displacements along the x direction.

keeping the other nodes' positions fixed, the potential deformation energy becomes a three-dimensional function of the displaced node's position:

$$\mathcal{U}_{\text{sys}} = \mathcal{U}_{\text{sys}}(\boldsymbol{r}_1, \boldsymbol{r}_2, \ldots, \boldsymbol{r}_7; \boldsymbol{r}) \equiv \mathcal{U}_{\text{sys}}(\boldsymbol{r}). \tag{14}$$

The resulting potential energy function, visualized in Figure 3b, is spherically symmetric given the symmetry of the micromechanical model. While this symmetry is broken once different nanocell types are introduced in the model, the symmetry observed here allows us to easily validate the force calculation, which is a vital part of `MicMec`. To this end, we compared the analytical expression of the forces, given in Eqs. 6 and 7, with the negative numerical gradient of the potential energy $\mathcal{U}_{\text{sys}}(\boldsymbol{r})$ of Figure 3b. As illustrated in Figure 3c, the numerical and analytical expressions coincide, illustrating that the micromechanical forces in the `MicMecForceField` module are implemented correctly.

Finally, we also validated that the bulk modulus of the micromechanical test system corresponds with the value that can be extracted from the predefined elastic stiffness tensor

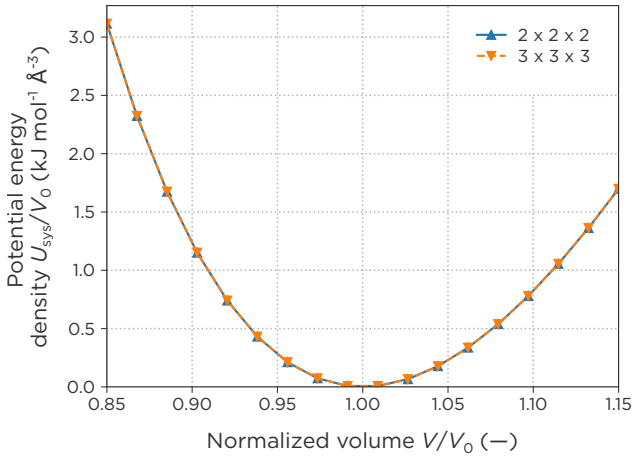

Figure 4: Potential deformation energy density, $\mathcal{U}_{\text{sys}}/V_0$, as a function of the normalized volume, V/V_0, for a $2 \times 2 \times 2$ and a $3 \times 3 \times 3$ micromechanical model containing nanocells of the 'test' type.

to check our implementation of the `Optimizer` module. From the postulated stiffness tensor $\mathbf{C}_0^{\text{test}}$, the bulk modulus follows as $K = (C_{0,11}^{\text{test}} + 2C_{0,12}^{\text{test}})/3 = 36.7$ GPa. To find the bulk modulus in the micromechanical model, energy scans as a function of the volume were performed for both a $2 \times 2 \times 2$ and a $3 \times 3 \times 3$ test system. For each volume point, the structure was rescaled isotropically from equilibrium and the micromechanical nodes were allowed to relax at this given volume. The resulting potential energy is depicted in Figure 4. For both system sizes, a quadratic fit to the ten data points between a normalized volume of 0.98 and 1.02 reveals a bulk modulus of 36.7 GPa, in agreement with the analytical value.

3.2 Scale-up in simulation timestep achieved by the micromechanical model

One of the main advantages of the micromechanical model—similar to other CG models—is that the high-frequency motions of the atomic system, such as O–H stretches, are removed by grouping atoms into massive beads. As a result, the frequency with which the forces on the system must be sampled, and hence the simulation timestep, can be increased compared to a typical value of 0.5–1.0 fs used in atomic simulations. The theoretical upper limit is

dictated by the Nyquist sampling theorem, which states that the maximum timestep in a simulation is given by half the period of the fastest motion in the sampled system. This value is typically taken as a rule of thumb, and actual sampling timesteps are about one order of magnitude smaller than the period of the fastest motion.

For our test system—whose parameters are in the same order of magnitude as realistic systems—we can approximate the slowest period $\Delta T_{\min}$ based on information on the unit cell length ($a = 10$ Å), the mass of the micromechanical nodes ($m = 10^7 m_e$), and the largest component of the stiffness tensor ($C_{\max}^{\text{test}} = 50$ GPa). This yields:

$$\Delta T_{\min} = \pi \sqrt{\frac{m_{\min}}{C_{\max} a}} = 1.34 \text{ ps}. \tag{15}$$

Similarly, this slowest period can also be deduced based on the elastic constant entering Hooke's law, $k_{\max}$, in Figure 3c:

$$\Delta T_{\min} = \pi \sqrt{\frac{m_{\min}}{k_{\max}}} = 0.79 \text{ ps}. \tag{16}$$

Both equations indicate that the smallest period lies in the picosecond range, pointing to a maximum simulation timestep of a few tenths of a picosecond. This would imply an increase in timestep compared to atomic simulations of about two to three orders of magnitude.

To verify this statement, we performed MD simulations of the $2 \times 2 \times 2$ micromechanical test system in the (N, V, E) ensemble. In this ensemble, the system's equations of motion are Hamiltonian in nature, defined by the Hamiltonian

$$\mathcal{H}_{\text{sys}}(\{\boldsymbol{r}_{klm}\}, \{\boldsymbol{p}_{klm}\}) = \sum_{klm} \frac{\boldsymbol{p}_{klm}^2}{2m_{klm}} + \sum_{\kappa\lambda\mu} \mathcal{U}_{\kappa\lambda\mu}(\{\boldsymbol{r}_{klm}\}). \tag{17}$$

In this expression, $\boldsymbol{p}_{klm} = m_{klm}\dot{\boldsymbol{r}}_{klm}$ and m_{klm} are the momentum and mass associated with the micromechanical node with indices (k, l, m), and $\mathcal{U}_{\kappa\lambda\mu}$ is the elastic deformation energy associated with the nanocell with indices (κ, λ, μ), as given in Eqs. 4 and 5. As the

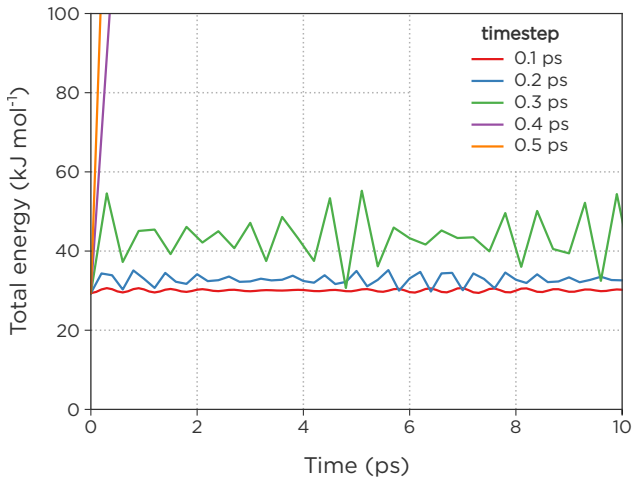

Figure 5: Total energy as a function of the simulation time for an (N, V, E) simulation of a $2 \times 2 \times 2$ micromechanical model containing nanocells of the 'test' type, with various timesteps.

microcanonical ensemble is dictated by a Hamiltonian, the total energy, being the sum of the kinetic and elastic potential energy, should be conserved during the simulation except for possible minor short-term deviations. Therefore, the actual maximum timestep that can be reached in a micromechanical simulation can be obtained by checking the maximum timestep for which the conserved energy is indeed conserved. To this end, we systematically increased the timestep Δt from 0.1 ps with increments of 0.1 ps and initiated short (N, V, E) MD simulations. As illustrated in Figure 5, increasing the timestep to 0.2 ps and even 0.3 ps only leads to short-term deviations in the total energy, without any long-term drift. Only when the timestep is increased to 0.4 ps or above, long-term drifts are observed, indicating that the maximum simulation timestep has been exceeded. Therefore, the maximum allowed timestep for this system amounts to *circa* 0.3 ps. Furthermore, the conservation of the total energy for lower timesteps validates the implementation of the `VerletIntegrator` module.

3.3 Equilibrium mechanics of correlated node defects in UiO-66

Before turning our attention to the mixed **reo**:**fcu** UiO-66 materials, we first confirmed that the elastic stiffness tensors of the pure **reo** and pure **fcu** materials are well reproduced by

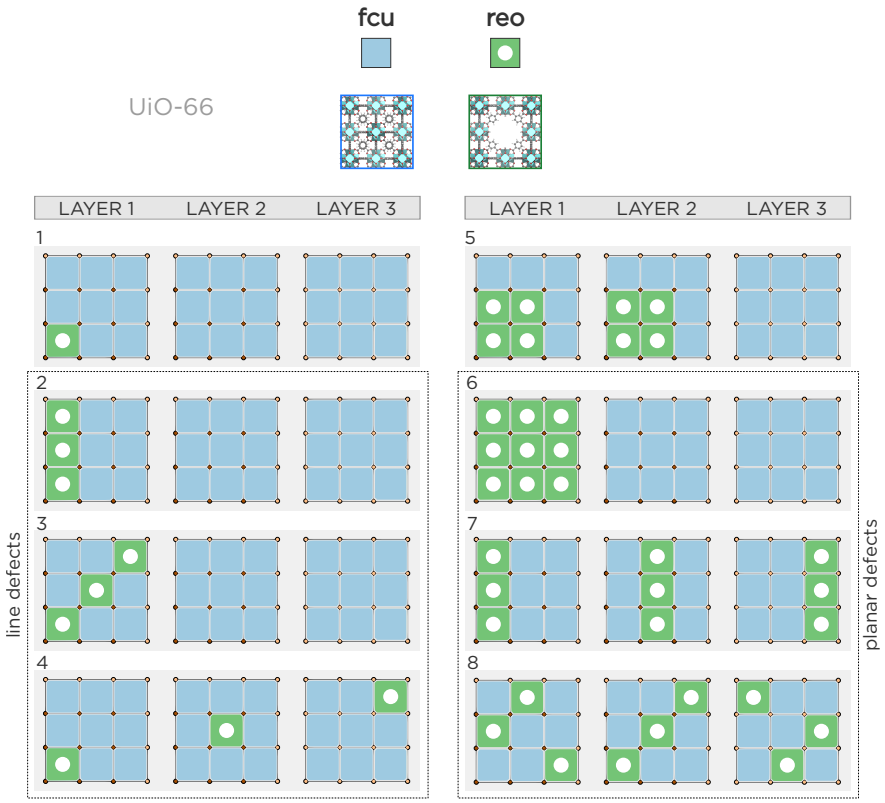

Figure 6: The eight $3 \times 3 \times 3$ **reo**:**fcu** configurations considered in this manuscript, with the atomic composition of each nanocell given in the top part of the figure. Layers 1, 2, and 3 are stacked on top of each other along the z direction.

the micromechanical model. As in the mixed configurations below, we considered a $3 \times 3 \times 3$ micromechanical model and determined the elastic stiffness tensors following the approach outlined in the computational details section. As presented in Section S3 of the Supporting Information, the elastic stiffness tensors of the $3 \times 3 \times 3$ micromechanical model simulations are in excellent agreement with those of the $3 \times 3 \times 3$ atomic simulations, as well as with the input elastic stiffness tensors presented in Eqs. 12 and 13.

Inspired by these results, we constructed a diverse set of eight mixed **reo**:**fcu** configurations each consisting of 27 nanocells, as illustrated in Figure 6. Configuration 1 consists of a single node-defective **reo** nanocell in an otherwise **fcu** material. Given the periodic boundary conditions, the location of this isolated **reo** nanocell is arbitrary. Configurations 2 to 4 correspond to three **reo** nanocells and 24 **fcu** nanocells, distributed in such a way that

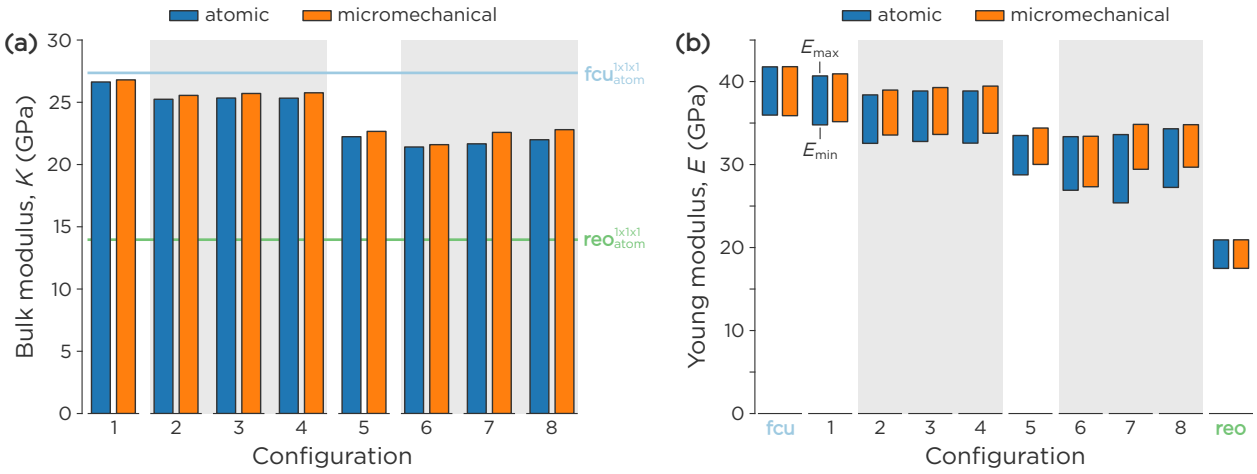

Figure 7: Equilibrium mechanical moduli of the different **reo**:**fcu** configurations. **(a)** Bulk modulus K for the eight configurations of Figure 6, calculated either atomically or with the micromechanical model. The bulk moduli of the atomistic **fcu** and **reo** systems are indicated with a horizontal line. **(b)** Range of directional Young modulus E for the eight configurations of Figure 6 as well as the $3 \times 3 \times 3$ homogeneous **fcu** and **reo** systems, calculated either atomically or with the micromechanical model.

they form a correlated line of node defects. This line is oriented along one of the periodic axes in configuration 2, a face diagonal in configuration 3, and a body diagonal in configuration 4. Configuration 5 consists of a $2 \times 2 \times 2$ cluster of eight correlated **reo** cells whose position within the larger $3 \times 3 \times 3$ micromechanical model is again arbitrary due to the periodic boundary conditions. Finally, configurations 6 to 8 correspond to correlated planes of nine node-defective **reo** cells, whose normal is oriented along one of the periodic axes in configuration 6, a face diagonal in configuration 7, and a body diagonal in configuration 8.

For all **reo**:**fcu** configurations, the full elastic stiffness tensors are tabulated and compared to their atomic counterparts in Section S3 of the Supporting Information. Figure 7 summarizes the most important elastic moduli: the bulk and the Young modulus. In all cases, good agreements are found between the atomic and the micromechanical results, with deviations that do not exceed a few percent. The bulk modulus visualized in Figure 7a decreases more or less linearly upon increasing **reo** content. For configurations 2, 3, and 4, as well as for configurations 6, 7, and 8, the orientation of the linear or planar **reo** defective

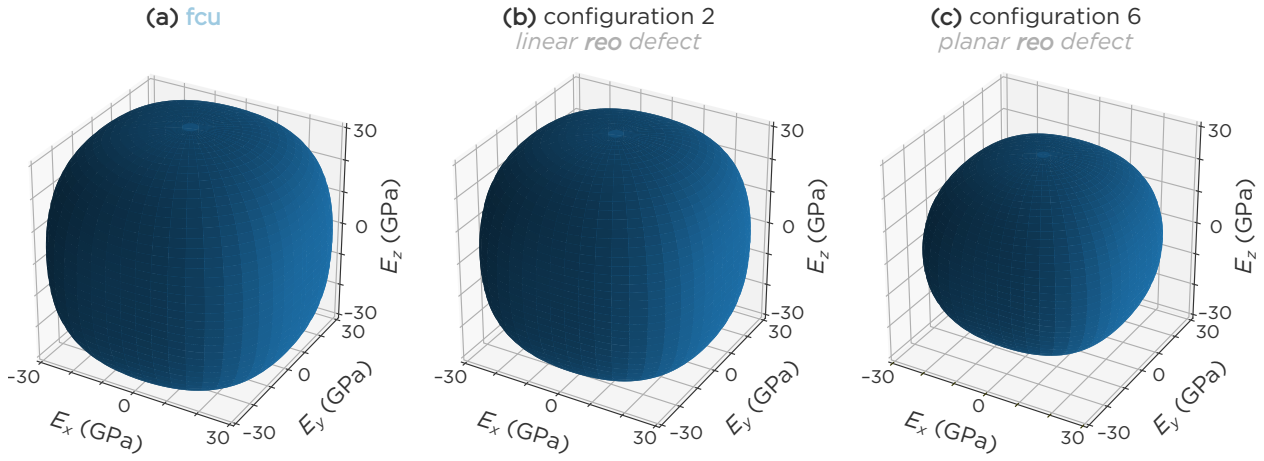

Figure 8: Directional Young modulus of **(a)** the **fcu** model, **(b)** configuration 2, containing a linear **reo** defect, and **(c)** configuration 6, containing a planar **reo** defect.

cells only induces minor variations in bulk modulus. While this is in line with the bulk modulus being a direction-averaged mechanical property, it is a significant result. For instance, while configurations 2, 3, and 4 correspond with line defects, two neighboring **reo** nanocells in the micromechanical model of configuration 2 share four nodes. In contrast, neighboring **reo** nanocells share two nodes and one node in configurations 3 and 4, respectively. These differences, which are induced by the discretization of the material into the micromechanical model, have only a minor effect on the obtained bulk modulus and support using the micromechanical model for this type of simulations.

The same conclusions can be drawn for the Young modulus visualized in Figure 7b. The Young modulus provides an even more stringent test for our `MicMec` implementation, as it is direction-dependent. Figure 7 shows, for each configuration, the different Young moduli the material exhibits when varying the direction along which the strain is applied, which coincides with the direction along which the stress is measured for the Young modulus. Of special attention are configurations 6, 7, and 8, for which a significantly larger spread is found between the material's minimum and maximum Young modulus compared to the other configurations.

To understand this phenomenon, Figure 8 visualizes the directional Young modulus for

the configuration 6 structure, containing a planar **reo** defect perpendicular to the z direction, alongside the ones for the homogeneous **fcu** model and configuration 2, containing a linear **reo** defect along the y direction. Compared to the defect-free structure, the Young modulus for configuration 2 shrinks isotropically, thereby largely retaining its anisotropy. Indeed, independent of the direction along which a strain is applied in configuration 2, the plane perpendicular to this direction contains sufficient **fcu** cells to counteract this strain. For configuration 6, this is different. When a strain is applied along the z direction, one of the layers perpendicular to this direction is completely composed of **reo** nanocells and will therefore compress more easily. This substantially lowers the Young modulus along this direction, while the Young modulus along other directions remains substantially larger. Also here, the micromechanical model succeeds in reproducing these fine mechanical details, outperforming the semiquantitative mechanical moduli obtained through traditional CG methods.[31,34] This excellent agreement between the atomic and micromechanical results is a direct consequence of relying on the unit cell matrices and—potentially anisotropic—elastic stiffness tensors in equilibrium as input parameters for the micromechanical model. This agreement also further adds to our model's validation on realistic materials.

4 Conclusions

Crucial to advancing computational material design is routine access to the model sizes needed to describe realistic disordered materials, such as MOF mixed matrix membranes, which may require simulation models in the micrometer range. To this end, in this work, we implemented the micromechanical model into the open-source `MicMec` software, discussed the main features of our implementation, and extensively validated it on both analytical systems and disordered **reo**:**fcu** UiO-66 structures. From a theoretical point of view, this implementation allowed us to properly define the elastic deformation energy, which lies at the heart of the forces acting on the micromechanical nodes in our model. In addition, we

demonstrated the importance of using different representations to construct a given nanocell matrix to capture the local motion of each individual micromechanical node. These representations systematically deal with the non-bijective connection between the micromechanical nodes and the micromechanical nanocells they define.

An analytical micromechanical test model was adopted to thoroughly verify the different core `MicMec` components: the connection between micromechanical nodes and nanocells in the `System` object, the definition of the elastic deformation energy and associated micromechanical forces in the `MicMecForceField` object, and the execution of both optimizations and molecular dynamics simulations in the `Optimizer` and `VerletIntegrator` objects, respectively. Besides passing each of these tests, this analytical model also demonstrated that the maximum allowed timestep in a micromechanical simulation amounts to a few tenths of a picosecond. As this is two to three orders of magnitudes larger than in an atomistic simulation, the micromechanical model provides access to phenomena occurring on correspondingly larger length and longer time scales.

Finally, we considered how the concentration and distribution of correlated node-defective **reo** cells within a defect-free **fcu** UiO-66 matrix affect the spatially disordered material's mechanical properties as a real-life example of our model. We observed that both the bulk and the Young moduli decrease with increasing **reo** content. Additionally, a larger spread between the material's maximum and minimum Young's modulus was observed in the case the **reo** defects cluster into layers, as this exposes weak directions in the material. An excellent agreement between the atomic and micromechanical elastic stiffness tensors was obtained for all systems under study, underpinning the veracity of our micromechanical predictions and improving on more traditional CG techniques.

In conclusion, we herein demonstrated the advantages and accuracy of the micromechanical model and provided our `MicMec` implementation as an open-source code at `https://github.com/Jlvdwall/micmec`. We hope this software may help the community to shed light on the role of spatial heterogeneities in real-life materials on yet unexplored length

scales, and this in a complementary and hierarchical fashion with both atomic simulations and macroscopic experiments.

Acknowledgement

J.S.D.V and S.M.J.R acknowledge the Fund for Scientific Research-Flanders (FWO) for a strategic basic (SB) research fellowship (grant no. 1S94521N) and a senior postdoctoral fellowship (grant no. 12T3522N), respectively. This work is furthermore supported by the Research Board of Ghent University (BOF). The computational resources (Stevin Supercomputer Infrastructure) and services used in this work were provided by VSC (Flemish Supercomputer Center), funded by Ghent University, FWO, and the Flemish Government—department EWI. We also thank prof. Veronique Van Speybroeck for insightful discussions on the topic.

Supporting Information Available

Validation of the expression for the deformation energy (Eq. 4), overview of the four core `MicMec` routines and of the `Micromechanical Model Builder` to create micromechanical systems as input for `MicMec`, and comparison of the atomistic and micromechanical stiffness tensors for the **reo**:**fcu** systems discussed in this work. This material is available free of charge via the Internet at `http://pubs.acs.org/`.

Data Availability.

Computational data supporting the results of this work are available from the online GitHub repository at `https://github.com/SvenRogge/supporting-info` or upon request from the authors.

Code Availability.

The `MicMec` software is freely available at `https://github.com/Jlvdwall/micmec`, with documentation at `https://jlvdwall.github.io/micmec/`.

References

(1) Simon, C. M.; Kim, J.; Gomez-Gualdron, D. A.; Camp, J. S.; Chung, Y. G.; Martin, R. L.; Mercado, R.; Deem, M. W.; D., G.; Haranczyk, M. et al. The materials genome in action: identifying the performance limits for methane storage. *Energy Environ. Sci.* **2015**, *8*, 1190–1199.

(2) Gaillac, R.; Pullumbi, P.; Coudert, F.-X. ELATE: an open-source online application for analysis and visualization of elastic tensors. *J. Phys. Condens. Matter* **2016**, *28*, 275201, https://progs.coudert.name/elate [Accessed: May 26, 2022].

(3) Shevlin, S.; Castro, B.; Li, X. Computational materials design. *Nat. Mater.* **2021**, *20*, 727.

(4) Friederich, P.; Häse, F.; Proppe, J.; Aspuru-Guzik, A. Machine-learned potentials for next-generation matter simulations. *Nat. Mater.* **2021**, *20*, 750–761.

(5) Marzari, N.; Ferretti, A.; Wolverton, C. Electronic-structure methods for materials design. *Nat. Mater.* **2021**, *20*, 736–749.

(6) Van Speybroeck, V.; Vandenhaute, S.; Hoffman, A. E. J.; Rogge, S. M. J. Towards modeling spatiotemporal processes in metal–organic frameworks. *Trends Chem.* **2021**, *3*, 605–619.

(7) Furukawa, H.; Cordova, K. E.; O'Keeffe, M.; Yaghi, O. M. The Chemistry and Applications of Metal–Organic Frameworks. *Science* **2013**, *341*, 1230444.

(8) Chen, Z.; Kirlikovali, K. O.; Li, P.; Farha, O. K. Reticular Chemistry for Highly Porous Metal–Organic Frameworks: The Chemistry and Applications. *Acc. Chem. Res.* **2022**, *55*, 579–591.

(9) Wei, Y.-S.; Zhang, M.; Ruqiang, Z.; Xu, Q. Metal-Organic Framework-Based Catalysts with Single Metal Sites. *Chem. Rev.* **2020**, *120*, 12089–12174.

(10) Bavykina, A.; Kolobov, N.; Khan, I. S.; Bau, J. A.; Ramirez, A.; Gascon, J. Metal-Organic Frameworks in Heterogeneous Catalysis: Recent Progress, New Trends, and Future Perspectives. *Chem. Rev.* **2020**, *120*, 8468–8535.

(11) Fan, W.; Zhang, X.; Kang, Z.; Liu, X.; Daofeng, D. Isoreticular chemistry within metal-organic frameworks for gas storage and separation. *Coord. Chem. Rev.* **2022**, *443*, 213968.

(12) Lin, R.-B.; Xiang, S.; Zhou, W.; Chen, B. Microporous Metal-Organic Framework Materials for Gas Separation. *Chem* **2020**, *6*, 337–363.

(13) Hanikel, N.; Prévot, M. S.; Yaghi, O. M. MOF water harvesters. *Nat. Nanotech.* **2020**, *15*, 348–355.

(14) Xu, W.; Yaghi, O. M. Metal–Organic Frameworks for Water Harvesting from Air, Anywhere, Anytime. *ACS Cent. Sci.* **2020**, *6*, 1348–1354.

(15) Liu, L.; Chen, Z.; Wang, J.; Zhang, D.; Zhu, Y.; Ling, S.; Huang, K.-W.; Belmabkhout, Y.; Adil, K.; Zhang, Y. et al. Imaging Defects and Their Evolution in a Metal-Organic Framework at Sub-unit-cell Resolution. *Nat. Chem.* **2019**, *11*, 622–628.

(16) Johnstone, D. N.; Firth, F. C. N.; Grey, C. P.; Midgley, P. A.; Cliffe, M. J.; Collins, S. M. Direct Imaging of Correlated Defect Nanodomains in a Metal–Organic Framework. *J. Am. Chem. Soc.* **2020**, *142*, 13081–13089.

(17) Sakata, Y.; Furukawa, S.; Kondo, M.; Hirai, K.; Horike, N.; Takashima, Y.; Uehara, H.; Louvain, N.; Meilikhov, M.; Tsuruoka, T. et al. Shape-Memory Nanopores Induced in Coordination Frameworks by Crystal Downsizing. *Science* **2013**, *339*, 193–196.

(18) Krause, S.; Bon, V.; Senkovska, I.; Többens, D. M.; Wallacher, D.; Pillai, R. S.; Maurin, G.; Kaskel, S. The Effect of Crystallite Size on Pressure Amplification in Switchable Porous Solids. *Nat. Commun.* **2018**, *9*, 1573.

(19) Rogge, S. M. J.; Waroquier, M.; Van Speybroeck, V. Unraveling the thermodynamic criteria for size-dependent spontaneous phase separation in soft porous crystals. *Nat. Commun.* **2019**, *10*, 4842.

(20) Abylgazina, L.; Senkovska, I.; Engemann, R.; Ehrling, S.; Gorelik, T. E.; Kavoosi, N.; Kaiser, U.; Kaskel, S. Impact of Crystal Size and Morphology on Switchability Characteristics in Pillared-Layer Metal-Organic Framework DUT-8(Ni). *Front. Chem.* **2021**, *9*, 674566.

(21) Lian, X.; Fang, Y.; Joseph, E.; Wang, Q.; Li, J.; Banerjee, S.; Lollar, C.; Wang, X.; Zhou, H.-C. Enzyme-MOF (metal-organic framework) composites. *Chem. Soc. Rev.* **2017**, *46*, 3386–3401.

(22) Chen, L.; Xu, Q. Metal-Organic Framework Composites for Catalysis. *Matter* **2020**, *1*, 57–89.

(23) Denny Jr., M. S.; Cohen, S. M. In Situ Modification of Metal-Organic Frameworks in Mixed-Matrix Membranes. *Angew. Chem. Int. Ed.* **2015**, *54*, 9029–9032.

(24) Dechnik, J.; Gascon, J.; Doonan, C. J.; Janiak, C.; Sumby, C. J. Mixed-Matrix Membranes. *Angew. Chem. Int. Ed.* **2017**, *56*, 9292–9310.

(25) Rogge, S. M. J. The micromechanical model to computationally investigate cooperative

and correlated phenomena in metal–organic framework. *Faraday Discuss.* **2021**, *225*, 271–285.

(26) Odoh, S. O.; Cramer, C. J.; Truhlar, D. G.; Gagliardi, L. Quantum-Chemical Characterization of the Properties and Reactivities of Metal–Organic Frameworks. *Chem. Rev.* **2015**, *115*, 6051–6111.

(27) Heinen, J.; Dubbeldam, D. On flexible force fields for metal–organic frameworks: Recent developments and future prospects. *Wire Comp. Mol. Sci.* **2018**, *8*, e1363.

(28) Unke, O. T.; Chmiela, S.; Sauceda, H. E.; Gastegger, M.; Poltavsky, I.; Schütt, K. T.; Tkatchenko, A.; Müller, K.-R. Machine Learning Force Fields. *Chem. Rev.* **2021**, *121*, 10142–10186.

(29) Eckhoff, M.; Behler, J. From Molecular Fragments to the Bulk: Development of a Neural Network Potential for MOF-5. *J. Chem. Theory Comput.* **2019**, *15*, 3793–3809.

(30) Noid, W. G. Perspective: Coarse-grained models for biomolecular systems. *J. Chem. Phys.* **2013**, *139*, 090901.

(31) Dürholt, J. P.; Galvelis, R.; Schmid, R. Coarse graining of force fields for metal–organic frameworks. *Dalton Trans.* **2016**, *45*, 4370–4379.

(32) Semino, R.; Dürholt, J. P.; Schmid, R.; Maurin, G. Multiscale Modeling of the HKUST-1/Poly(vinyl alcohol) Interface: From an Atomistic to a Coarse Graining Approach. *J. Phys. Chem. C* **2017**, *121*, 21491–21496.

(33) Jin, J.; Pak, A. J.; Durumeric, A. E. P.; Loose, T. D.; Voth, G. A. Bottom-up Coarse-Graining: Principles and Perspectives. *J. Chem. Theory Comput.* **2022**, *18*, 5759–5791.

(34) Alvares, C. M. S.; Maurin, G.; Semino, R. Coarse Grained modeling of Zeolitic Imidazolate Framework-8 using MARTINI Force Fields. 2023; `https://arxiv.org/abs/2302.04263`, [Accessed: March 5, 2023].

(35) Evans, J. D.; Coudert, F.-X. Macroscopic Simulation of Deformation in Soft Microporous Composites. *J. Phys. Chem. Lett.* **2017**, *8*, 1578–1584.

(36) Moghadam, P. Z.; Rogge, S. M. J.; Li, A.; Chow, C.-M.; Wieme, J.; Moharrami, N.; Aragones-Anglada, M.; Conduit, G.; Gomez-Gualdron, D. A.; Van Speybroeck, V. et al. Structure-Mechanical Stability Relations of Metal–Organic Frameworks via Machine Learning. *Matter* **2019**, *1*, 219–234.

(37) Ray, J. R.; Rahman, A. Statistical Ensembles and Molecular Dynamics Studies of Anisotropic Solids. *J. Chem. Phys.* **1984**, *80*, 4423–4428.

(38) Tadmor, E. B.; Miller, R. E.; Elliott, R. S. *Continuum Mechanics and Thermodynamics (From Fundamental Concepts to Governing Equations)*; Cambridge University Press, New York, 2011.

(39) Triguero, C.; Coudert, F.-X.; Boutin, A.; Fuchs, A. H.; Neimark, A. V. Mechanism of Breathing Transitions in Metal–Organic Frameworks. *J. Phys. Chem. Lett.* **2011**, *2*, 2033–2037.

(40) Triguero, C.; Coudert, F.-X.; Boutin, A.; Fuchs, A. H.; Neimark, A. V. Understanding adsorption-induced structural transitions in metal-organic frameworks: From the unit cell to the crystal. *J. Chem. Phys.* **2012**, *137*, 184702.

(41) Cavka, J. H.; Jakobsen, S.; Olsbye, U.; Guillou, N.; Lamberti, C.; Bordiga, S.; Lillerud, K. P. A New Zirconium Inorganic Building Brick Forming Metal Organic Frameworks with Exceptional Stability. *J. Am. Chem. Soc.* **2008**, *130*, 13850–13851.

(42) Valenzano, L.; Civalleri, B.; Chavan, S.; Bordiga, S.; Nilsen, M. H.; Jakobsen, S.; Lillerud, K. P.; Lamberti, C. Disclosing the Complex Structure of UiO-66 Metal Organic Framework: A Synergic Combination of Experiment and Theory. *Chem. Mater.* **2011**, *23*, 1700–1718.

(43) Shearer, G. C.; Forselv, S.; Chavan, S.; Bordiga, S.; Mathisen, K.; Bjørgen, M.; Svelle, S.; Lillerud, K. P. In Situ Infrared Spectroscopic and Gravimetric Characterisation of the Solvent Removal and Dehydroxylation of the Metal Organic Frameworks UiO-66 and UiO-67. *Top. Catal.* **2013**, *56*, 770–782.

(44) Wu, H.; Chua, Y. S.; Krungleviciute, V.; Tyagi, M.; Chen, P.; Yildirim, T.; Zhou, W. Unusual and Highly Tunable Missing-Linker Defects in Zirconium Metal–Organic Framework UiO-66 and Their Important Effects on Gas Adsorption. *J. Am. Chem. Soc.* **2013**, *135*, 10525–10532.

(45) Cliffe, M. J.; Wan, W.; Zou, X.; Chater, P. A.; Kleppe, A. K.; Tucker, M. G.; Wilhelm, H.; Funnell, N. P.; Coudert, F.-X.; Goodwin, A. L. Correlated Defect Nanoregions in a Metal–Organic Framework. *Nat. Commun.* **2014**, *5*, 4176.

(46) Shearer, G. C.; Chavan, S.; Ethiraj, J.; Vitillo, J. G.; Svelle, S.; Olsbye, U.; Lamberti, C.; Bordiga, S.; Lillerud, K. P. Tuned to Perfection: Ironing Out the Defects in Metal–Organic Framework UiO-66. *Chem. Mater.* **2014**, *26*, 4068–4071.

(47) Øien, S.; Wragg, D.; Reinsch, H.; Svelle, S.; Bordiga, S.; Lamberti, C.; Lillerud, K. P. Detailed Structure Analysis of Atomic Positions and Defects in Zirconium Metal–Organic Frameworks. *Cryst. Growth Des.* **2014**, *14*, 5370–5372.

(48) Trickett, C. A.; Gagnon, K. J.; Lee, S.; Gándara, F.; Bürgi, H.-B.; Yaghi, O. M. Definitive Molecular Level Characterization of Defects in UiO-66 Crystals. *Angew. Chem. Int. Ed.* **2015**, *54*, 11162–11167.

(49) Fang, Z.; Bueken, B.; De Vos, D. E.; Fischer, R. A. Defect-Engineered Metal–Organic Frameworks. *Angew. Chem. Int. Ed.* **2015**, *54*, 7234–7254.

(50) Burtch, N. C.; Heinen, J.; Bennett, T. D.; Dubbeldam, D.; Allendorf, M. D. Mechanical Properties in Metal–Organic Frameworks: Emerging Opportunities and Challenges for Device Functionality and Technological Applications. *Adv. Mater.* **2017**, *30*, 1704124.

(51) Born, M. On the Stability of Crystal Lattices. I. *Math. Proc. Cambridge Philos. Soc.* **1940**, *36*, 160–172.

(52) Mouhat, F.; Coudert, F.-X. Necessary and Sufficient Elastic Stability Conditions in Various Crystal Systems. *Phys. Rev. B* **2014**, *90*, 224104.

(53) Rogge, S. M. J.; Yot, P. G.; Jacobsen, J.; Muniz-Miranda, F.; Vandenbrande, S.; Gosch, J.; Ortiz, V.; Collings, I. E.; Devautour-Vinot, S.; Maurin, G. et al. Charting the Metal-Dependent High-Pressure Stability of Bimetallic UiO-66 Materials. *ACS Materials Lett.* **2020**, *2*, 438–445.

(54) Verstraelen, T.; Vanduyfhuys, L.; Vandenbrande, S.; Rogge, S. M. J. *Yaff, Yet Another Force Field*, Available online at http://molmod.ugent.be/software/ [Accessed: May 26, 2022].

(55) Shang, S.; Wang, Y.; Liu, Z.-K. First-Principles Elastic Constants of α- and θ-Al_2O_3. *Appl. Phys. Lett.* **2007**, *90*, 101909.

TOC Graphic

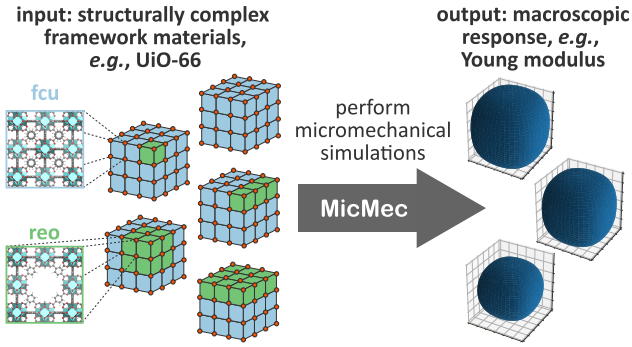
input: structurally complex framework materials, *e.g.*, UiO-66
fcu
reo
perform micromechanical simulations
MicMec
output: macroscopic response, *e.g.*, Young modulus